Numerical investigations of wave loads on fixed box in front of vertical wall with a narrow gap under wave actions

Junliang Gao[1, 2], Zhiwei He[1], Jun Zang[2 *], Qiang Chen[2], Haoyu Ding[2], Gang Wang[3]

1. School of Naval Architecture and Ocean Engineering, Jiangsu University of Science and Technology, Zhenjiang 212003, China

2. Research Unit for Water, Environment and Infrastructure Resilience (WEIR), Department of Architecture and Civil Engineering, University of Bath, BA2 7AY, U.K.

3. College of Harbour, Coastal and Offshore Engineering, Hohai University, Nanjing 210098, China

Abstract:

Violent fluid oscillations may appear inside the narrow gap between multiple structures in close proximity and cause severe damage to such structures and safe operations. Here, based on the OpenFOAM® package, this paper presents a numerical investigation of wave loads during gap resonance between a fixed box and a vertical wall by utilizing a two-dimensional (2D) numerical wave flume. The box-wall system is subjected to incident regular waves with various wave heights and frequencies. The topographies of plane slopes with various inclinations are arranged in front of the vertical wall. This paper focuses on the influences of the topographical variation on the wave loads, including the horizontal wave force, the vertical wave force and the moment on the box. It is found that all the frequencies, at which the maximum horizontal wave force, the maximum vertical wave force and the maximum moment appear, decrease with the increase of topographical slope, *S*, overall. Moreover, these frequencies are also shown to deviate from the fluid resonant frequency to different degrees. For all the incident wave heights considered, both the maximum horizontal wave force and the maximum moment present a pattern of fluctuation with the topographical slope.

Keywords: Fluid resonance; Narrow gap; Wave loads; Topographical effects; OpenFOAM®

* Corresponding author. E-mail: J.Zang@bath.ac.uk.

1. Introduction

In the last two decades, investigations on multiple structures in close proximity have aroused great interest in the marine engineering industry around the world because of their wide applications. For instance, when the liquefied natural gas (LNG) production is transferred from the floating liquefied natural gas (FLNG) platforms to liquefied natural gas carriers (LNGC), FLNG unit and the LNGC are usually arranged side-by-side in close proximity (Feng and Bai, 2015; Sun et al., 2015). Violent fluid oscillations maybe appear inside these narrow gaps under conditions of some wave frequencies, and hence cause the significant increase of hydrodynamic loads on structures when compared to the hydrodynamic loads on the same structure in isolation (Miao et al., 2001; Zhu et al., 2005). This kind of phenomenon is often called "*gap resonance*". It may cause excessive motions of the vessels moored side-by-side in close proximity (Chua et al., 2018; Perić and Swan, 2015) and may also result in the wave overtopping on the wharf/deck (Gao et al., 2019a). These hydrodynamic issues greatly affect the loading/offloading efficiency and even seriously threaten the safety of engineering operations. Therefore, more relevant investigations should be implemented to further enhance the knowledge on gap resonance.

Various research methods, including physical experiments, analytical analyses and numerical simulations, have been employed in the study of gap resonance. At the early stage, the research relied primarily on the analytical analyses based on the classical linear potential flow theory (e.g., Miao et al. (2001); Molin et al. (2002)). Subsequently, a number of physical experiments were further performed to improve the understanding of gap resonance and to examine previous analytical analyses. Saitoh et al. (2006), Iwata et al. (2007) and Tan et al. (2014) implemented a series of 2D laboratory experiments in wave flumes to investigate the fluid resonance inside narrow gaps formed by multiple fixed boxes or in a narrow gap formed by a fixed box in front of a vertical wall. Recently, some three-dimensional (3D) physical experiments of the gap resonance between two closely spaced structures or inside the moonpool were also carried out (e.g., Huang et al. (2020); Perić and Swan (2015); Zhao et al. (2017)).

The majority of numerical investigations heretofore utilized the classical potential flow model (e.g., Feng and Bai (2017); Li et al. (2005); Li and Zhang (2016); Sun et al. (2010)). Extensive comparisons have proved that the classical potential flow model is able to estimate the fluid resonant frequency well (the so-called fluid resonant frequency refers to the wave frequency

corresponding to the maximum amplification of free-surface elevation inside the narrow gap). Unfortunately, it was reported to remarkably over-predict the resonant wave height inside the gap and consequently cause the overestimation of the wave load on the structure. To address this issue, several special numerical methodologies have been proposed to suppress this unrealistic over-prediction (e.g., Chen (2004); Lu et al. (2010b); Newman (2004); Ning et al. (2015); Tan et al. (2019)). Nevertheless, for these special methodologies, there always exist unknown dissipative coefficients. These unknown coefficients have to be calibrated by using experimental data, and there is no a priori theory to determine them. In addition, it was found that different values of dissipative coefficients have to be separately employed for the wave load on the structure and for the fluid response inside the gap, even for the same wave conditions and structures (Liu and Li, 2014; Tan et al., 2014).

In nearly a decade, the CFD-based viscous flow numerical models have gradually become an effective alternative tool in the research of gap resonance. By adopting a finite element based Navier-Stokes numerical model with the CLEAR-VOF method, Lu et al. (2010a) investigated the fluid resonance response inside two narrow gaps between three identical fixed boxes subjected to normally-incident waves. Subsequently, Moradi et al. (2015) employed the OpenFOAM® model to investigate the effects of gap inlet shape on fluid resonance inside a narrow gap of two fixed bodies. Recently, also based on OpenFOAM®, various hydrodynamic problems on the gap resonance were further investigated by many scholars (e.g., Feng et al. (2017); Gao et al. (2019c); Jiang et al. (2018); Jiang et al. (2019b)).

Although a large number of investigations have been carried out on gap resonance, most of them were concerned about the fluid resonance inside narrow gaps between multiple fixed/floating bodies and the corresponding wave forces acting on them (e.g., Feng and Bai (2017); Gao et al. (2019c); Jiang et al. (2019a); Lu et al. (2010a); Moradi et al. (2015); Ning et al. (2016); Ning et al. (2018); Zhu et al. (2017)). The research on the fluid resonance inside the narrow gap formed between a large ship and a wharf is relatively rare. By utilizing physical experiments and numerical simulations, Wang and Zou (2007) investigated the fluid resonance inside a narrow gap between a fixed ship section and a bottom-mounted vertical quay in shallow water. Based on a semi-analytical analysis and physical experiments, Tan et al. (2014) studied the energy dissipative influences of resonant waves inside a narrow gap formed by floating box in front of vertical wall.

Subsequently, Perić and Swan (2015) experimentally studied the gap response between a ship-shaped vessel and a bottom-mounted box. Recently, by utilizing a numerical wave flume based on OpenFOAM®, Jiang et al. (2019b) systematically studied the influence of fluid viscosity and flow rotation on the gap resonance between a ship section and a bottom mounted terminal. In all these investigations, the influences of the variation of the topography in front of the vertical quay/wall on gap resonance were not considered because the seabed was always set to be flat.

Considering that in most situations the topographies in real harbors are normally non-flat and the water depth in front of wharf is usually changeable (Diaz-Hernandez et al., 2015; Gao et al., 2016a; Gao et al., 2016b; Gao et al., 2019b; Kumar and Gulshan, 2018; Wang et al., 2013), Gao et al. (2019a) investigated the effects of the topographic variation on the fluid resonance inside a narrow gap formed by a fixed box and a vertical wall for the first time. The fluid resonant frequency, the resonant wave height amplification and the reflection coefficient of the box-wall system were systematically investigated. It was found that all these parameters are closely related to the topographical variation in front of the vertical wall. Nevertheless, another important aspect, i.e., the wave loads acting on the structure, was not taken into consideration in that paper. Since the fluid resonance inside the gap presents the close dependence on the topography in front of the vertical wall, it is expected that the remarkable influences of the topographical variation on the wave loads would be observed. This is the main motivation of the current study.

This article is a direct extension of the numerical investigations in Gao et al. (2019a). In this article, the influences of the topographical variation on the wave loads acting on the box (including the horizontal wave force, the vertical wave force and the moment) are investigated in a 2D numerical wave flume based on OpenFOAM®. Although the hydrodynamic features of wave loads on the box might share some similarities with those of fluid resonance revealed in Gao et al. (2019a), some differences between them are expected and will be highlighted in this work.

The rest of this paper is organized as follows. Section 2 introduces the numerical model utilized in the current study. Section 3 describes the numerical wave flume and the incident wave conditions considered. In Section 4, the numerical model is verified against available experimental data. The numerical results and discussions are presented in Section 5. Finally, conclusions based on the results are drawn in Section 6.

2. Numerical model description

2.1. Governing equations

A two-phase flow solver "*interFoam*" built in OpenFOAM® is employed for all numerical simulations. The governing equations for the mass and momentum conservations are formulated as:

$$\frac{\partial \rho}{\partial t} + \frac{\partial \rho u_i}{\partial x_i} = 0, \tag{1}$$

$$\frac{\partial \rho u_i}{\partial t} + \frac{\partial \rho u_i u_j}{\partial x_j} = -\frac{\partial p}{\partial x_i} - g_i x_i \frac{\partial \rho}{\partial x_j} + \mu \frac{\partial}{\partial x_j}\left(\frac{\partial u_i}{\partial x_j} + \frac{\partial u_j}{\partial x_i}\right), \tag{2}$$

where ρ, u_i , p, μ and g_i denote the fluid density, the fluid velocity, the dynamic pressure, the fluid dynamic viscosity and the acceleration due to gravity, respectively. The governing equations are solved for both phases (i.e., water and air) simultaneously, and the interface between the two phases is captured by adopting a scalar field α which takes a value of 1 for water and 0 for air and intermediate values for a mixture of water and air.

In the VOF (Volume of Fluid) method, the distribution of α is calculated by the following advection equation:

$$\frac{\partial \alpha}{\partial t} + \frac{\partial \alpha u_i}{\partial x_i} + \frac{\partial \alpha (1-\alpha) u_{ir}}{\partial x_i} = 0, \tag{3}$$

where u_{ir} is the relative velocity between air and water. In this article, the contour of the α function with the value of 0.50 is used as the interface between the two phases. Based on the fraction indicator α, the spatial variation of the fluid density and the dynamic viscosity can be computed via the following weighting:

$$\rho = (1-\alpha)\rho_{\text{air}} + \alpha \rho_{\text{water}}, \tag{4}$$

$$\mu = (1-\alpha)\mu_{\text{air}} + \alpha \mu_{\text{water}}, \tag{5}$$

where the subscripts "air" and "water" refer to the fluid property of air and water, respectively.

2.2. Boundary conditions and numerical implementations

The "*waves2Foam*" toolbox proposed by Jacobsen et al. (2012) is used to generate the incident waves at the boundaries and avoid the wave re-reflection in the numerical wave flume (see Fig. 1). The velocity at the wave inlet boundary is specified as that of regular waves, and the pressure gradient at the boundary is set to zero. A relaxation zone is arranged in the vicinity of the

inlet boundary to dissipate the reflected waves from the box-wall system. The boundary condition at the upper side of the wave flume is set as "atmosphere", where the Dirichlet and Neumann types of boundary conditions are respectively prescribed to the pressure and velocity. At the right and bottom sides of the flume and the walls of the box, "no-slip" boundary condition is applied, which ensures zero normal and tangential velocities at these boundaries. For a 2D problem, the boundary condition at the front and back boundaries is set to "empty" for which no solution is required in the *y*-axis direction.

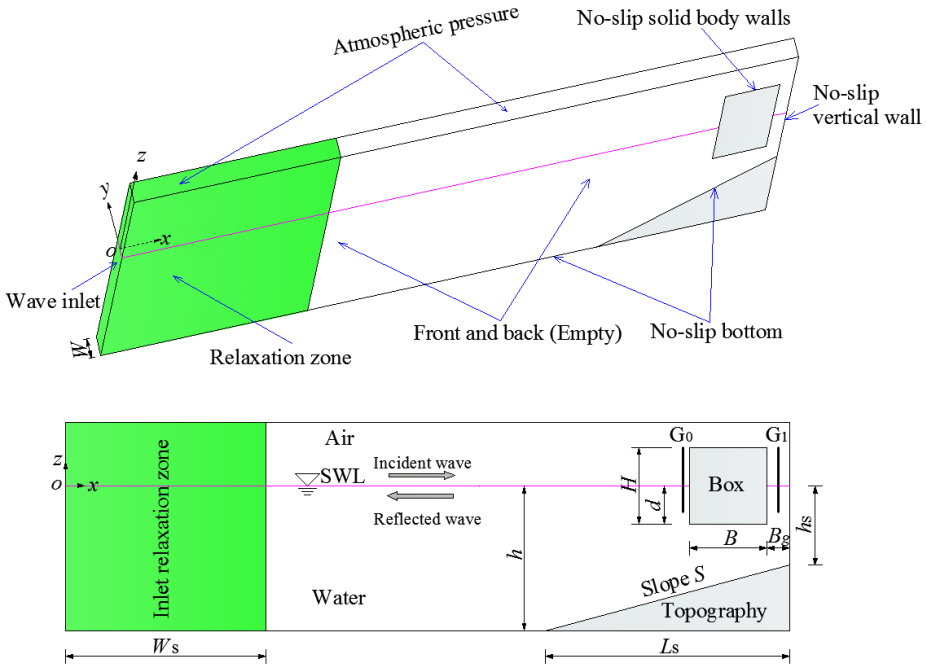

Fig. 1. Sketch of the numerical wave flume: (a) boundary conditions and the coordinate system; (b) the definition of the geometric parameters.

Eqs. (1)-(3) are solved by using the finite volume method. The time derivatives are discretized by a first-order Euler scheme. The gradient terms are approximated by the Gaussian integration method that is based on a linear interpolation from cell centers to cell faces, and the divergence terms are evaluated by the Gauss Convection-specific schemes. The velocity and pressure are decoupled by the PISO (Pressure Implicit with Splitting of Operators) algorithm (Jasak, 1996). Identical to Feng et al. (2017); Moradi et al. (2015), to ensure obtaining accurate and stable numerical results, the largest Courant number in all simulations is set to 0.25; if it exceeds this value for some cells, the time step will be reduced automatically. Once the above

equations are solved, the wave load on the structure can be obtained by integrating pressure and shear stress on the wet solid surface of the box at each time step. In the current work, the moment acting on the box corresponds to its centroid.

3. Numerical wave flume

The 2D numerical wave flume employed in all simulations is illustrated in Fig. 1 The length and the height of the wave flume are 14.0 m and 0.8 m, respectively. Its thickness in the y-axis direction is set to W=0.1 m, which corresponds to one computational cell. In this article, the ship section is simplified as a square shape cross-section, and only a fixed box with the breadth of B=0.5 m, the height of H=0.5 m and the draft of d=0.25 m in front of a vertical wall is investigated. A narrow gap with the width of B_g=0.05 m is formed between the box and the wall. The water depth at the region from x=0 to x=12.0 m is a constant, h=0.5 m. While at the region from x=12.0 m to x=14.0 m (i.e., L_s=2.0 m), there exists a plane-slope topography beneath the box. Six different water depths in front of the wall (namely, h_s=0.5 m, 0.45 m, 0.40 m, 0.35 m, 0. 30 m and 0.27 m) are considered; equivalently, the topographical slopes, $S=(h-h_s)/L_s$, are equal to 0, 0.025, 0.050, 0.075, 0.100 and 0.113. The air depth in the whole wave flume is a constant, h_a=0.3 m. To record the wave fields around the box, two wave gauges G_1 and G_2 are deployed. G_1 is placed very close to the left side of the box and the distance between them is only 0.005 m. G_2 is arranged in the middle of the gap.

Regular waves with various frequencies and wave heights are produced at the wave inlet boundary by using the second-order Stokes wave theory. The wave frequency, ω, varies from 2.514 rad/s to 5.586 rad/s; correspondingly, the dimensionless wavenumber, kh, varies from 0.6 to 1.7 ($k=2\pi/L$ denotes the wavenumber and L denotes the incident wavelength). Five different incident wave heights (i.e, H_0=0.005 m, 0.024 m, 0.050 m, 0.075 m and 0.100 m) are considered. The relaxation zone arranged near the wave inlet boundary has a width of W_s=8.0 m. The length of 8.0 m is about 1.53 times of the maximum wavelength corresponding to the incident waves with ω=2.514 rad/s, which ensures that the relaxation zone can effectively absorb the reflected waves from the box-wall system for all simulations.

The numerical wave flume shown in Fig. 1 is discretized by using two mesh generation utilities built in OpenFOAM®. First, by using the "*blockMesh*" utility, a structured hexahedral

background mesh is produced. To track the free water surface accurately, the cell size in the vertical direction gradually becomes smaller from the bottom/atmosphere sides to the still water level. In addition, finer cells with smaller horizontal sizes are arranged around the box, especially inside the narrow gap, to accurately simulate the wave fields there. Then, by employing the "*snappyHexMesh*" utility, the boundaries of the fixed box and the topography are generated by subtracting the desired volumes from the background mesh. A typical computational mesh is presented in Fig. 2, where the topography with S = 0.113 is taken as an example.

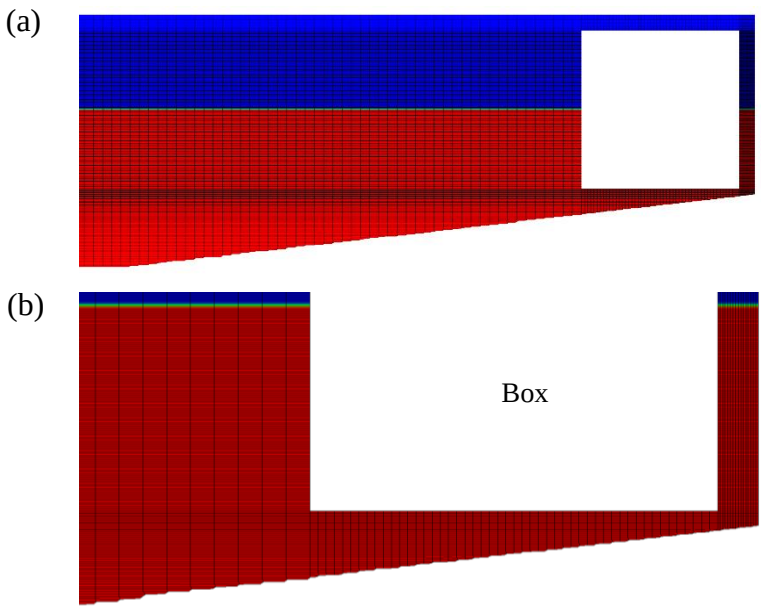

Fig. 2. Typical meshes in the computational domain: (a) the meshes above the topography; (b) the meshes around the box (taking the topography with S = 0.113 as an example)

Table 1. Details of three meshes with different resolutions under the condition of S=0

Mesh	Nos. of the cell, face & point ($\times 10^3$)			No. of the cell across the gap	
	Cell	Face	Point	Along the *z*-axis	Along the *x*-axis
Coarse	117	466	239	240	20
Medium	204	817	411	280	26
Fine	282	1128	567	330	34

In general, for hydrodynamic problems, the CFD-based simulation results are broadly affected by the mesh employed. In this article, three different meshes, namely the coarse, medium

and fine meshes, are utilized to examine the influences of the mesh density on the wave loads acting on the box. For the topography with S=0, the detailed information for these three meshes is presented in Table 1. For the other five topographies (i.e., S=0.025, 0.050, 0.075, 0.100 and 0.113), the numbers of the cell, point and face for the three meshes become slightly lower than those for the topography with S=0 because the cells beneath the slope are removed.

Based on the simulation results of the horizontal wave forces that will be shown in Section 5.1, when the incident waves have a wave height of H_0=0.005 m, for the topographies with S=0 and 0.113, the maximum horizontal wave forces inside the narrow gap occurs at kh=1.350 and 0.840, respectively. For the case with H_0=0.005 m, S=0 and kh=1.350, the dependence of the maximum horizontal wave force and the corresponding vertical wave force and moment on the mesh resolution is presented in Fig. 3, in which $A_0=H_0/2$ refers to the amplitude of the incident waves. Moreover, to further check the mesh convergence of the numerical results for the topography with $S \neq 0$, the maximum horizontal wave force and the corresponding vertical wave force and moment for the case with H_0=0.005 m, S=0.113 and kh=0.840 are illustrated in Fig. 4. It can be observed that for both cases, the time histories of all wave loads (including the horizontal wave force, the vertical wave force and the moment) for the three meshes are almost identical to each other, which indicates that the numerical results of the wave loads are insensitive to the selected meshes. Considering the computational cost and the numerical accuracy, the medium mesh is employed in all simulations. A total time of 40.0 s is simulated for all cases. It is seen from Figs. 3 and 4 that all the wave loads have achieved a steady state at t = 20 s. All the results which will be presented in Section 5 are based on the steady-state time histories of the wave loads from 20 s to 40 s.

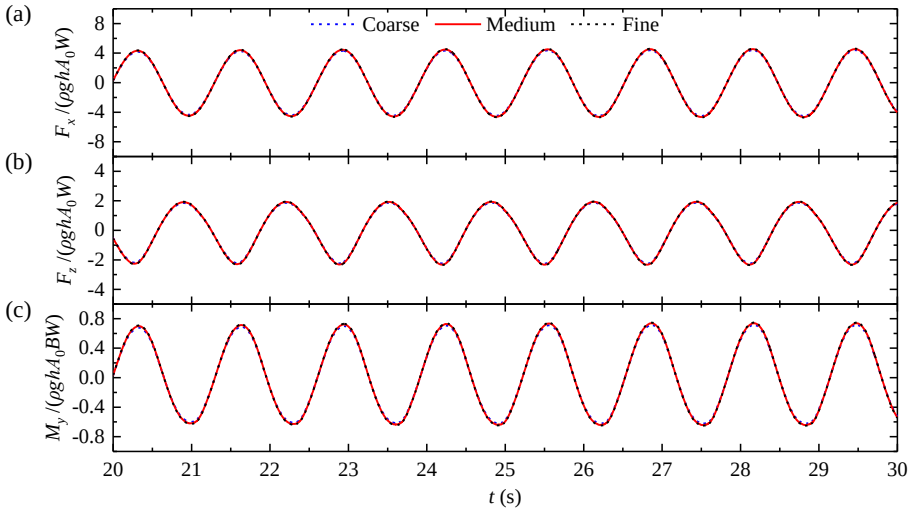

Fig. 3. Dependence of the wave loads on the mesh resolution for the case with H_0=0.005 m, S=0 and kh=1.350: (a)-(c) correspond to the horizontal wave force, the vertical wave force and the moment, respectively. A_0=H_0/2 in the figure denotes the amplitude of the incident waves.

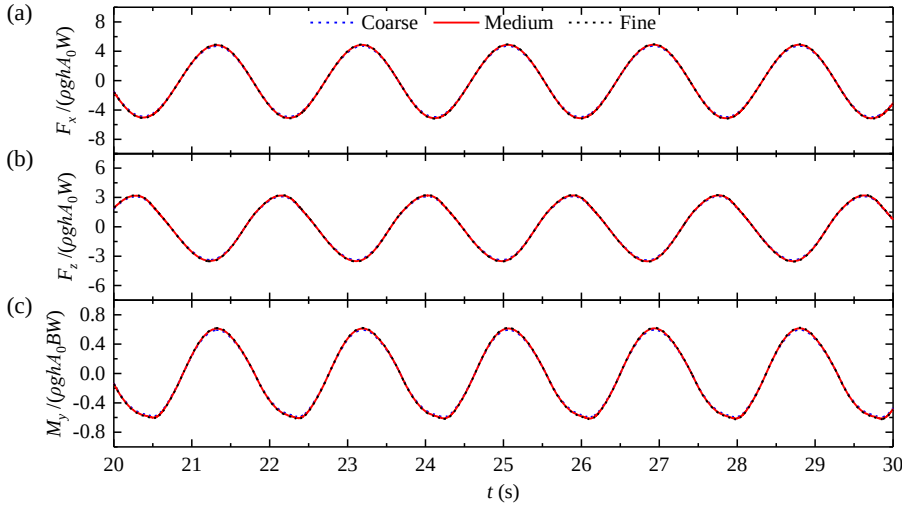

Fig. 4. Dependence of the wave loads on the mesh resolution for the case with H_0=0.005 m, S=0.113 and kh=0.840: (a)-(c) correspond to the horizontal wave force, the vertical wave force and the moment, respectively.

4. Numerical model validation

By reproducing the physical experiments of for wave evolutions during passage over a submerged bars under various wave conditions, the capacity of the OpenFOAM® model in predicting the wave transformation over an uneven seabed has been well validated in the literature

(e.g., Morgan and Zang (2011); Morgan et al. (2010)). In this section, the capacity of OpenFOAM® in predicting the free-surface elevations and the wave loads during gap resonance is further examined. Wang and Zou (2007) conducted a set of laboratory experiments to investigate the fluid resonance phenomenon inside a gap between a ship section and a vertical quay wall. The free-surface elevations at different locations, the wave pressure and the wave forces on the ship section were also measured in their experiments.

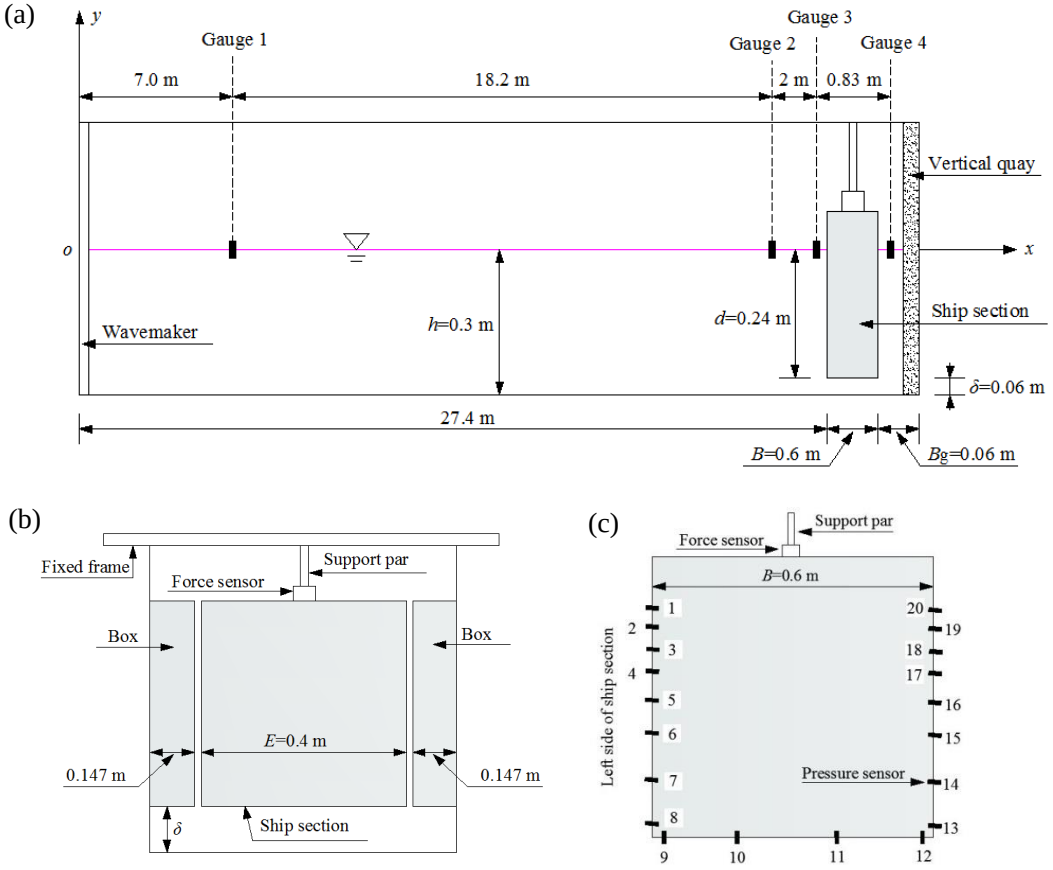

Fig. 5. Setups for the physical experiments of Wang and Zou (2007): (a) longitudinal section of the wave flume; (b) cross-section of the wave flume; (c) pressure probe setup

Detailed experimental setups for the physical model tests of Wang and Zou (2007) are illustrated in Fig. 5. The experiments were performed in a wave flume with a length of 46 m, a width of 0.7 m and a height of 1.0 m. A wavemaker was arranged at one end of the wave flume to generate the incident waves. The ship section model had a length of B=0.6 m, a width of E=0.4 m and a height of 0.45 m. It was deployed 27.4 m away from the wavemaker and was fixed by a support bar. The vertical quay wall was deployed 0.06 m away from the ship section. Two boxes

with a width of 0.147 m were positioned at the two lateral sides of the ship section model. Between the two boxes and the ship section, there existed two gaps with a width of 0.003 m to avoid the friction between them. The free-surface elevations were measured by four wave gauges shown in Fig. 5a. The horizontal and vertical wave forces on the ship section were measured by the force sensor that was arranged in the middle of the ship section (see Fig. 5b and c). Twenty pressure probes were fixed on the ship bottom and on the two sides of the ship section to measure the wave pressure on the surface of the ship section (see Fig. 5c). Four of them were deployed on the ship bottom, eight of them on the left side of the ship section, and eight of them on the right side. The locations of all these pressure probes are listed in Table 2.

Table 2. Positions of the pressure probes deployed in the experiments of Wang and Zou (2007)

No. of pressure probe	1	2	3	4	5	6	7	8
Distance from ship bottom (m)	0.30	0.27	0.24	0.21	0.18	0.13	0.08	0.02
No. of pressure probe	9		10		11		12	
Distance from the left side of ship (m)	0.02		0.2		0.4		0.58	
No. of pressure probe	13	14	15	16	17	18	19	20
Distance from ship bottom (m)	0.02	0.08	0.13	0.18	0.21	0.24	0.27	0.30

In the laboratory experiments, cnoidal and sine wave trains were generated by the wavemaker, and four cases (two for cnoidal waves and two for sine waves) were investigated. In this section, only the two cases for sine waves (i.e., Cases 2 and 4 in Wang and Zou (2007)) are reproduced by the numerical model, and Table 3 presents the incident wave parameters used in Wang and Zou (2007) for the two cases. It should be noted that in our simulations, the wave heights of the incident sine waves employed in numerical simulations are determined by means of accurately reproducing the free-surface elevation at gauge 1. In order to accurately match the numerical free-surface elevation at gauge 1 with the experimental data, the configuration of the numerical wave flume is set to be identical to that of the physical experiments shown in Fig. 5a. Different from the numerical tank shown in Fig. 1, no relaxation zone is deployed at the wave inlet boundary here. The numerical simulations are terminated when the reflected waves from the ship-wall system arrive at the wave inlet boundary. A mesh configuration that has a similar mesh density with the medium mesh described in Section 3 is utilized, and the

number of the computational cells in the mesh is 413200.

Table 3. Incident wave characteristics used in Wang and Zou (2007) for Cases 2 and 4

Case	Wave type	Wave height H_0 (m)	H_0/h	Wave period T (s)	$T\sqrt{g/h}$
2	Sine wave	0.06	0.2	3	17.1
4	Sine wave	0.06	0.2	5	28.5

Fig. 6 shows the comparisons of the experimental and simulated the free-surface elevations at the four wave gauges for Cases 2 and 4. It is seen that for both cases and for all the wave gauges, the free-surface elevations predicted by the numerical model are well consistent with the experimental data. This indicates that not only the incident wave trains at gauge 1 but also the wave fields in front of the ship section and inside the narrow gap are accurately reproduced by the present numerical model. The simulated wave pressures on the surface of the ship section are further shown in Fig. 7. Because only the time histories of the wave pressures for Case 4 were presented in Wang and Zou (2007), only the comparisons of the experimental and simulated wave pressures for Case 4 are illustrated in this figure. The pressure probes 8 and 13 are respectively placed on the left and the right sides of the ship section, and the pressure probes 9-12 are deployed on the ship bottom. The simulated wave pressures at all these pressure probes are also shown to be in good agreement with the experimental data. Finally, the comparisons of the experimental and simulated wave forces on the ship section for Cases 2 and 4 are presented in Fig. 8. Due to that the wave pressures have been well simulated by the numerical model, as expected, the wave forces (including the horizontal and vertical forces) are also shown to be accurately predicted by the model. The good agreement between the numerical results and the experimental data shown in Figs. 6-8 indicates that the OpenFOAM® model can accurately predict not only free-surface elevations but also wave pressures and wave forces on the structure for the gap resonance problem formed by the box-wall system.

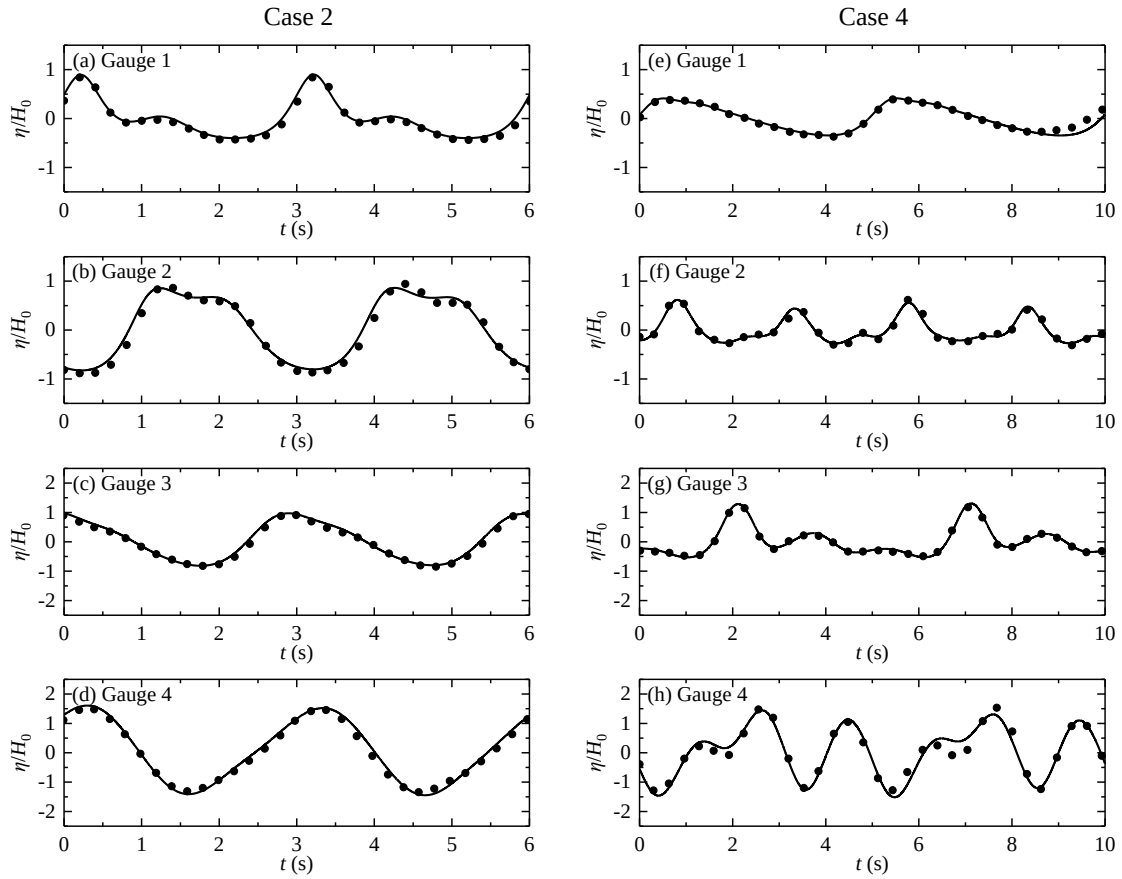

Fig. 6. Time histories of the free-surface elevations at various wave gauges. (a)-(d) correspond to Case 2; (e)-(h) correspond to Case 4. (Lines: the simulation results; dots: the experimental data)

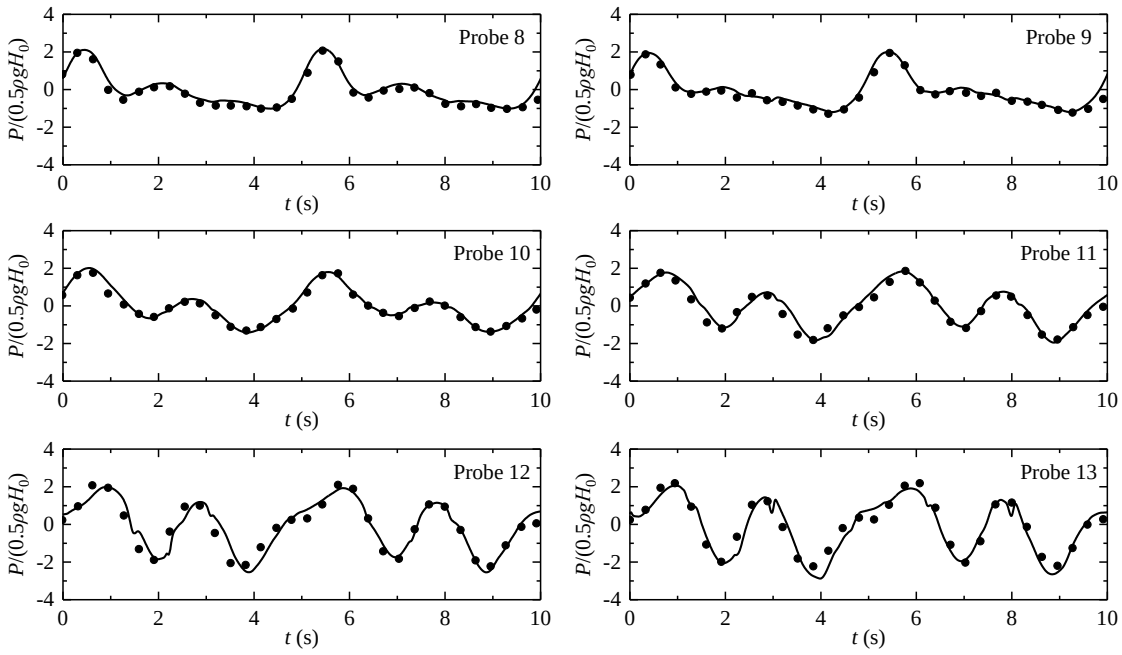

Fig. 7. Time histories of wave pressures at various pressure probes for Case 4. (Lines: the

simulation results; dots: the experimental data)

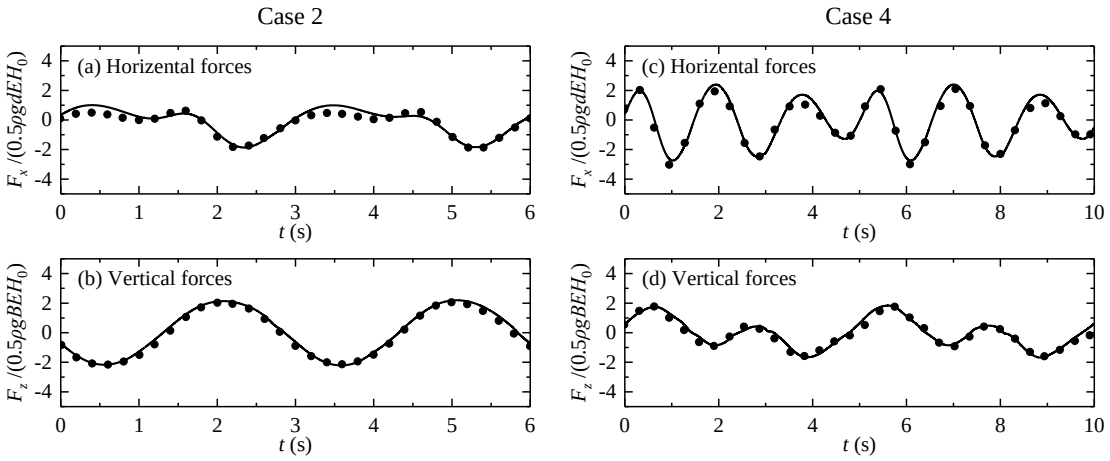

Fig. 8. Time histories of the wave forces on the ship section. (a) and (b) correspond to Case 2; (c) and (d) correspond to Case 4. (Lines: the simulation results; dots: the experimental data)

5. Numerical results and discussion

For the numerical setup described in Section 3, the influences of the topographical variation on the fluid resonant frequency, the resonant wave height inside the gap and the reflection coefficient from the box-wall system has been systematically studied in Gao et al. (2019a). In this section, the issues about how the topographical variation affects the wave loads acting on the box (including the horizontal wave force, the vertical wave force and the moment) are further investigated. The similarities and differences between the characteristics of the fluid resonance inside the gap and the wave loads on the box are also highlighted.

5.1. Horizontal wave force on the box

Fig. 9 illustrates the variations of the amplitude of the horizontal wave force, $\bar{F}_x$, with respect to the wave frequency for various topographies and incident wave heights. It should be noted that the black and red vertical dash lines in the figure refer to the fluid resonant frequency, $(kh)_{Hg}$, and the frequency at which the maximum horizontal wave force appears, $(kh)_{Fx}$, for the topography with S=0.113, respectively. The values of $(kh)_{Hg}$ under these topographies and incident wave heights are given in Gao et al. (2019a). There are two obvious phenomena that can be found from this figure. Firstly, for all the incident wave heights considered in this paper, the frequency at

which the maximum horizontal wave force appears, $(kh)_{Fx}$, always decreases with the increase of the topographical slope, S. To present the phenomenon better, the variation of $(kh)_{Fx}$ with respect to the slope, S, is further illustrated in Fig. 10. It is seen that in general the value of $(kh)_{Fx}$ decreases gradually with the increase of the slope, S. This is similar to the variation tendency of the fluid resonant frequency with respect to the slope, which indicates that the wave field inside the gap has a dominating effect on the horizontal wave force on the box.

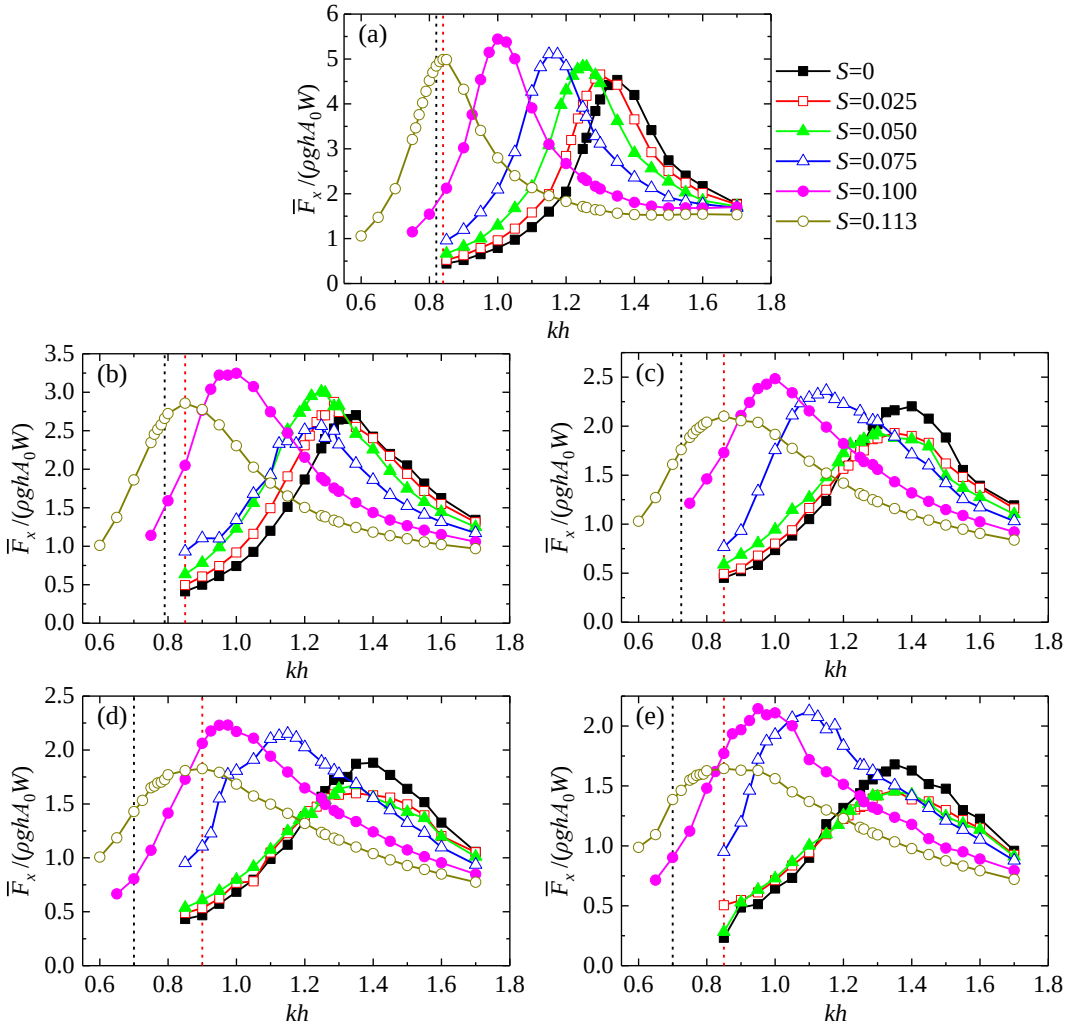

Fig. 9. Variations of the amplitude of the horizontal wave force, $\overline{F}_x$, with respect to the wave frequency under the conditions of various topographies and incident wave heights. (a)-(e) correspond to H_0=0.005 m, 0.024 m, 0.050 m, 0.075 m and 0.100 m, respectively. The black and red vertical dash lines refer to the fluid resonant frequency and the frequency at which the maximum horizontal force appears for S=0.113, respectively.

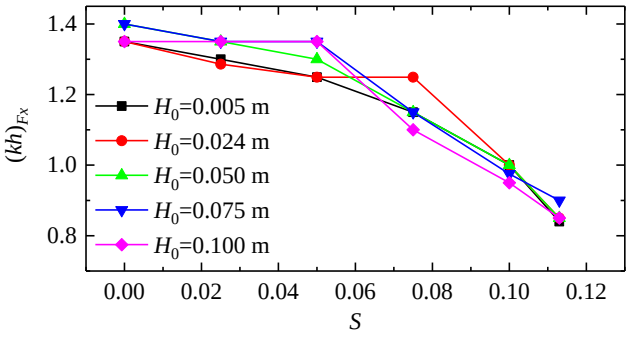

Fig. 10. The variation of the frequency at which the maximum horizontal wave force appears, $(kh)_{Fx}$, with respect to the topographical slope, S.

Secondly, for the topography with S=0.113, there exist obvious deviations between the frequency at which the maximum horizontal force appears, $(kh)_{Fx}$ and the fluid resonant frequency, $(kh)_{Hg}$, regardless of the incident wave height being small or large. In fact, for the other topographies, similar phenomenon can also be observed. To show this phenomenon more intuitively and comprehensively, the differences between $(kh)_{Fx}$ and $(kh)_{Hg}$ for all cases are demonstrated in Fig. 11. It can be seen that for the overwhelming majority of the cases, the value of $(kh)_{Fx}$ is always larger than that of $(kh)_{Hg}$; only two cases show the equality of $(kh)_{Fx}$ and $(kh)_{Hg}$. In addition, it can also be found from this figure that the deviation degree between $(kh)_{Fx}$ and $(kh)_{Hg}$ for H_0=0.005 m is obviously less than that for the larger incident wave heights (i.e., H_0=0.024 m, 0.050 m, 0.075 m and 0.100 m).

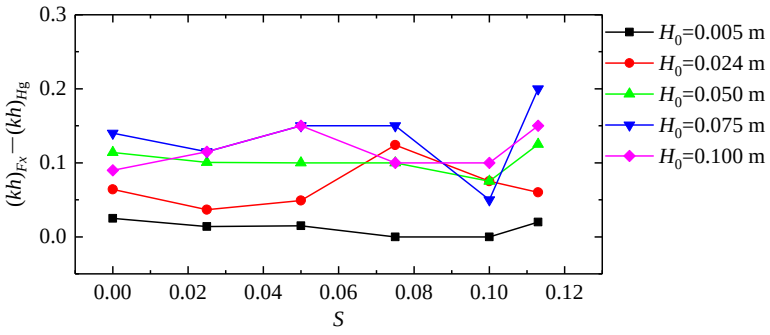

Fig. 11. The differences between $(kh)_{Fx}$ and $(kh)_{Hg}$ for all cases, in which $(kh)_{Hg}$ denote the fluid resonant frequency.

The phenomena presented in Figs. 10 and 11 can be explained as follows. According to Lu et al. (2011), the horizontal wave force on the box is highly dependent on the water level difference

between the opposite sides of the body and can be qualitatively expressed as

$$F_x(t) = C(\psi_1^2 - \psi_2^2). \tag{6}$$

The symbol C in this equation is a proportionality constant, $\psi_i = \eta_i + d$ (i=1 and 2), and η_i is the free-surface elevation at gauge G_i. Through simple mathematical transformation, the above equation can be further formulated as

$$F_x(t) = D(\eta_1 - \eta_2 + \frac{\eta_1^2}{2d} - \frac{\eta_2^2}{2d}), \tag{7}$$

in which D=2dC is also a proportionality constant. Hence, via comparing the relative magnitudes of the four items in the brackets, all these phenomena can be reasonably explained.

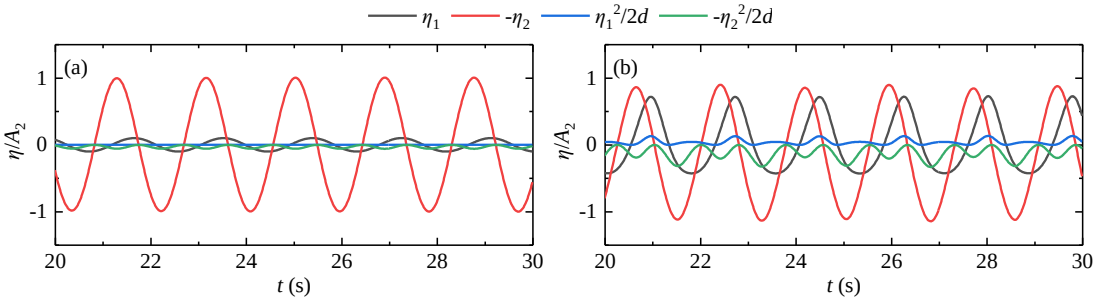

Fig. 12. Comparisons of the time histories of the four terms shown in the brackets of Eq. (7) for two cases with (a) H_0=0.005 m, S=0.113, kh=0.84 and (b) H_0=0.075 m, S=0.113, kh=0.90. The symbol η in this figure presents η_1, $-\eta_2$, $\eta_1^2/2d$ or $-\eta_2^2/2d$, and A_2 denotes the amplitude of η_2.

Take two cases with S=0.113 for example. One has the parameters of H_0=0.005 m and kh=0.84; the other has H_0=0.075 m and kh=0.90. It is seen from Fig. 9a and d that both cases possess the maximum horizontal wave forces for their corresponding incident wave heights. Fig. 12 presents the comparisons of the time histories of the four terms shown in the brackets of Eq. (7) for these two cases. It is noted that the time histories of them are all normalized by A_2 which denotes the amplitude of η_2. It is seen that for both cases, the term of $-\eta_2$ always has the maximum relative magnitude compared to the other three terms (i.e., η_1, $\eta_1^2/2d$ and $-\eta_2^2/2d$), which proves the above statement that the wave field inside the gap has a dominating effect on the horizontal wave force on the box. Meanwhile, it can also be observed that although the term of $-\eta_2$ always has the maximum relative magnitude, the horizontal wave force is also modulated by

the other three terms, which explains why there exist deviations between $(kh)_{Fx}$ and $(kh)_{Hg}$. In addition, for different incident wave heights, the other three terms have different modulation degrees. For H_0=0.005 m (see Fig 12a), due to the fact that the amplifications of the free surfaces inside the gap are significantly larger than those for the larger incident wave heights (Gao et al., 2019a), the modulation effect of the other three terms is extremely limited and the horizontal wave force is almost entirely determined by $-\eta_2$. Hence, the deviation degree between $(kh)_{Fx}$ and $(kh)_{Hg}$ for H_0=0.005 m is obviously less than that for the larger incident wave heights.

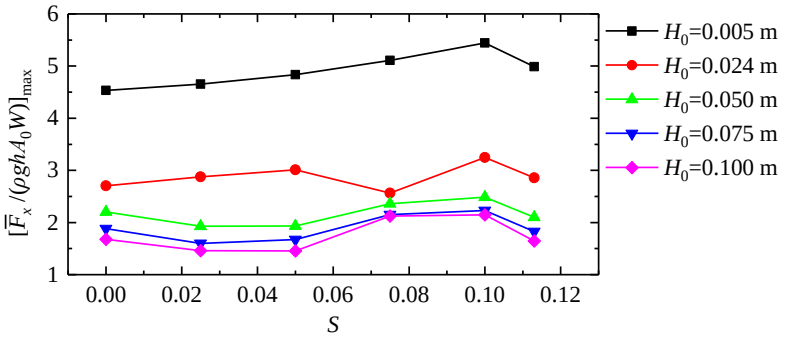

Fig. 13. The variation of the maximum horizontal wave force with respect to the topographical slope, *S*.

Fig. 13 shows the variations of the maximum horizontal wave force with respect to the topographical slope. It can be observed that for all the incident wave heights, the maximum horizontal wave force presents a pattern of fluctuation with the topographical slope. Besides, for each incident wave height, the variation curve of the maximum horizontal wave force is shown to coincide well with the variation of the amplification of resonant wave height with respect to the topographical slope shown in Gao et al. (2019a). This further indicates that the wave field inside the gap has a dominating influence on the horizontal wave force on the box. Moreover, it can also be found that for all the topographies, the dimensionless maximum horizontal wave forces, $[\bar{F}_x/(\rho g h A_0 W)]_{\max}$, decrease gradually with the increase of the incident wave height, which is also completely consistent with the corresponding finding for the amplification of resonant wave height.

5.2. Vertical wave force on the box

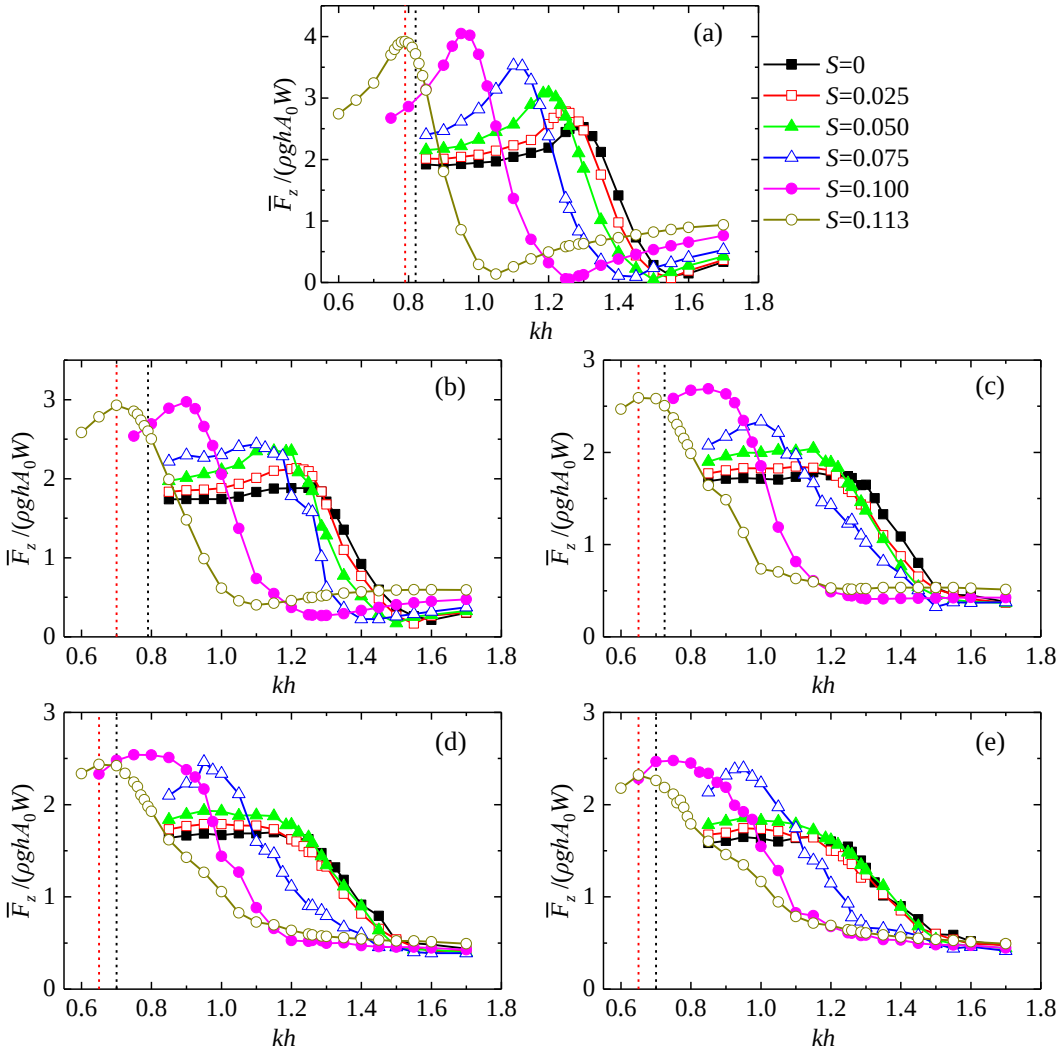

Fig. 14. Variations of the amplitude of the vertical wave force, $\bar{F}_z$, with respect to the wave frequency under the conditions of various topographies and incident wave heights. (a)-(e) correspond to H_0=0.005 m, 0.024 m, 0.050 m, 0.075 m and 0.100 m, respectively. The black and red vertical dash lines refer to the fluid resonant frequency and the frequency at which the maximum vertical force appears for S=0.113, respectively.

Fig. 14 presents the variations of the amplitude of the vertical wave force, $\bar{F}_z$, with respect to the wave frequency for various topographies and incident wave heights. The black and red vertical dash lines shown in this figure refer to the fluid resonant frequency, $(kh)_{Hg}$, and the frequency at which the maximum vertical wave force appears, $(kh)_{Fz}$, for the topography with S=0.113, respectively. The following four phenomena can be intuitively observed from this figure. Firstly,

for all the incident wave heights, the frequency at which the maximum vertical wave force appears, $(kh)_{Fz}$, always decreases with the increase of the topographical slope, S. To demonstrate the phenomenon better, the variation of $(kh)_{Fz}$ with the slope, S, is further presented in Fig. 15. Similar to the frequency $(kh)_{Fx}$, the magnitude of $(kh)_{Fz}$ also decreases gradually with the increase of the slope, S, overall. This indicates that the wave field inside the gap has a great impact upon the vertical wave force as well.

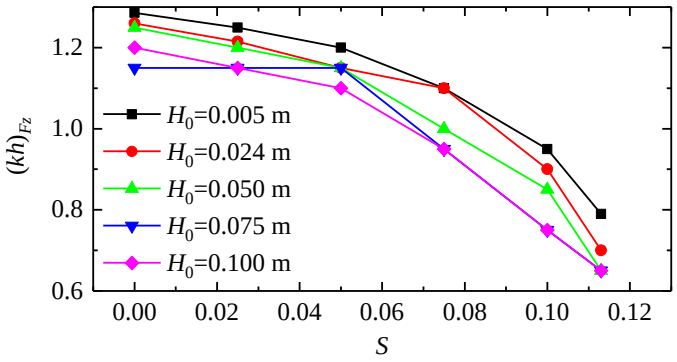

Fig. 15. The variation of the frequency at which the maximum vertical wave force appears, $(kh)_{Fz}$, with respect to the topographical slope, S.

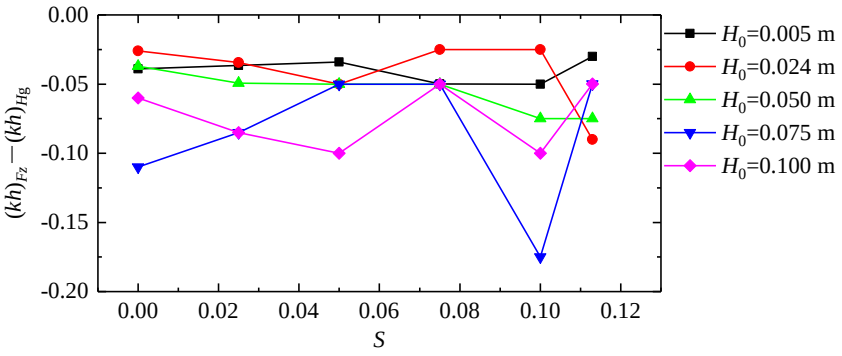

Fig. 16. The differences between $(kh)_{Fz}$ and $(kh)_{Hg}$ for all cases

Secondly, for the topography with S=0.113, similar to the frequency $(kh)_{Fx}$, there also exist obvious deviations between the frequency at which the maximum vertical wave force appears, $(kh)_{Fz}$ and the fluid resonant frequency, $(kh)_{Hg}$, no matter whether the incident wave height is small or large. For the other topographies, similar phenomenon can also be observed. It should be noted that, when the incident wave height is relatively large and the topographical slope is relatively small (see Fig. 14c-e), the vertical wave force seems to become insensitive to the wave frequency

when the wave frequency is less than a certain critical value. Under this condition, $(kh)_{Fz}$ refers to that critical wave frequency. However, different from $(kh)_{Fx}$ that tends to be larger than $(kh)_{Hg}$, $(kh)_{Fz}$ is shifted to a lower value compared with $(kh)_{Hg}$. To illustrate this phenomenon more comprehensively, the differences between $(kh)_{Fz}$ and $(kh)_{Hg}$ for all cases are further presented in Fig. 16. It is seen that the values of $(kh)_{Fz}-(kh)_{Hg}$ are always shown to be negative, which indicates that the values of $(kh)_{Fz}$ are always less than the corresponding values of $(kh)_{Hg}$ for all the topographies and incident wave heights considered in this paper.

Thirdly, it can also be seen from Fig. 14 that for all the incident wave heights, larger topographical slope tends to result in larger maximum vertical wave force. Fig. 17 further shows the variations of the maximum vertical wave force with respect to the topographical slope, S, for all the incident wave heights. As mentioned above, the vertical wave force becomes insensitive to the wave frequency when the wave frequency is less than a certain critical value under the conditions of larger incident wave heights and smaller topographical slopes (see Fig. 14c-e). In these circumstances, the maximum vertical wave force shown in Fig. 17 refers to the averaged value of those vertical wave forces that are insensitive to the wave frequency. It can be observed from Fig. 17 that when $S \leq 0.100$, the maximum vertical wave force increases obviously with the increase of the topographical slope. When the topographical slope further increases up to S=0.113, the maximum vertical wave force only decreases slightly compared with that when S=0.100.

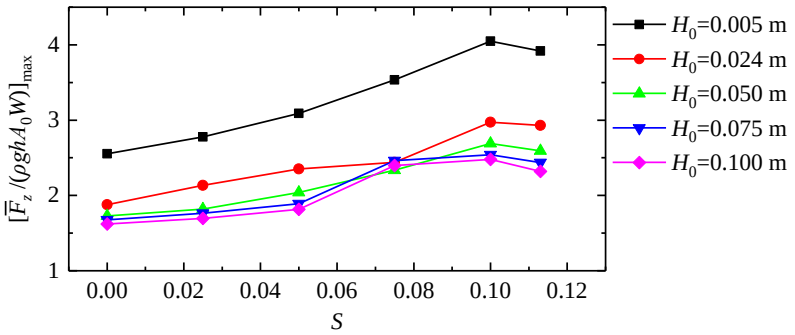

Fig. 17. The variation of the maximum vertical wave force with respect to the topographical slope, S.

Fourthly, observing Fig. 14 can also easily find that for a certain set of the incident wave height and the topography (especially for a smaller wave height and a larger slope), apart from a

maximum vertical wave force, there exists a minimum one. To reveal the reasons why the maximum and minimum vertical forces occur, Fig. 18 presents comparisons of the time histories of the vertical wave forces with those of the free-surface elevations at gauges G_1 and G_2 for the two cases with kh=0.79 and 1.05 under conditions of H=0.005 m and S=0.113. These two cases respectively possess the maximum and minimum vertical forces for the given incident wave height and topography. t_0 in this figure refers to one of the moments that crests of the vertical wave force appear, T denotes the incident wave period, and η presents η_1 or η_2. The distributions of the dynamic pressure p around the box for the two cases in some typical moments are further presented in Fig. 19.

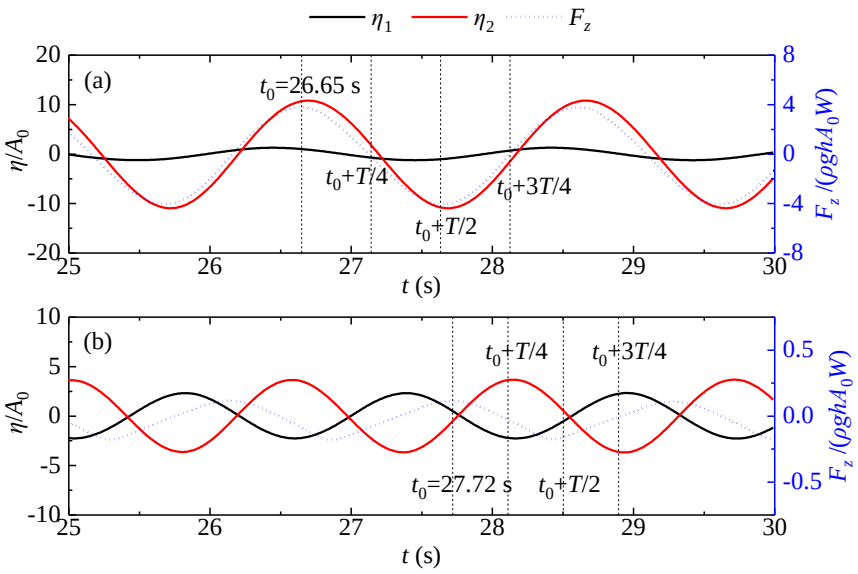

Fig. 18. Time histories of the vertical wave forces and the free-surface elevations at gauges G_1 and G_2 for the two cases with (a) kh=0.79 and (b) kh=1.05 under conditions of H=0.005 m and S=0.113. t_0 refers to one of the moments that crests of the vertical wave force appear, T denotes the incident wave period, and η presents η_1 or η_2.

For the case with kh=0.79 (Fig. 18a), it is seen that the magnitude of η_2 is much greater than that of η_1. In addition, η_2 and F_z are almost in-phase. Both phenomena indicate that the wave field inside the gap has almost decisive influence on the vertical wave force when the fluid resonance occurs. Fig. 19a and c shows that when the free surface in the gap approaches its maximum or minimum elevation, the positive or negative pressure is distributed among the whole bottom of the

box, which indicates the decisive influence of the wave field inside the gap more intuitively. For the case with kh=1.05 (Fig. 18b), it is observed that η_1 and η_2 have similar magnitudes but are almost anti-phase. This will inevitably result in the simultaneous existence of the positive and negative dynamic pressure along the bottom of the box, which can be proved by observing Fig. 19c and d. Since the vertical wave force is the result of integrating the dynamic pressure along the whole bottom of the box, the obvious pressure anti-phases in different parts of the bottom will produce smaller vertical wave forces.

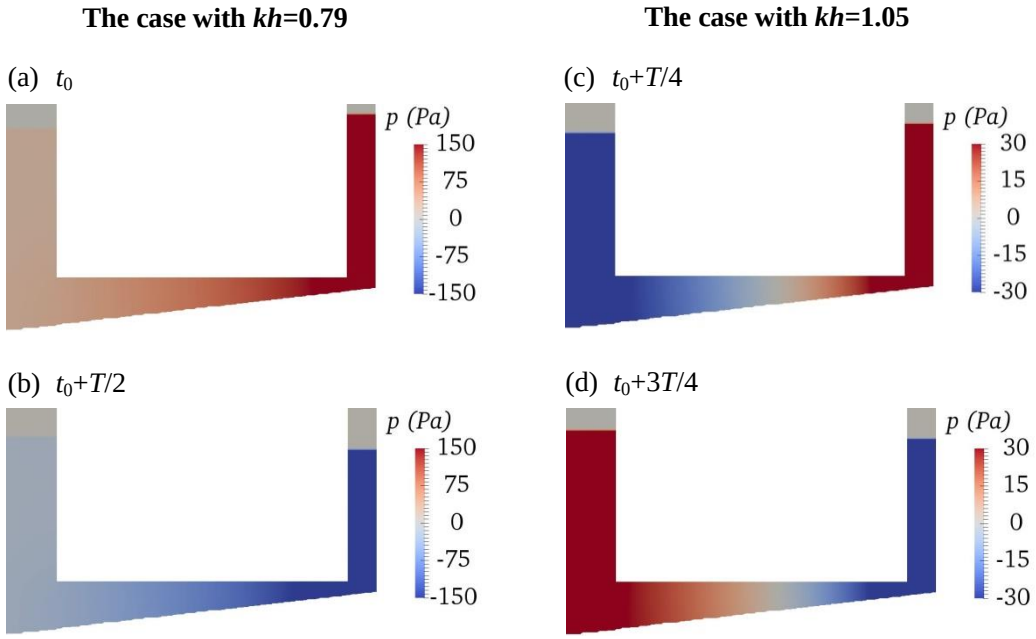

Fig. 19. Distributions of the dynamic pressure p around the box for the two cases presented in Fig. 18. (a) and (b) correspond to the moments of t_0 and t_0+T/2 for the case with kh=0.79; (c) and (d) correspond to the moments of t_0+T/4 and t_0+3T/4 for the case with kh=1.05.

5.3. Moment on the box

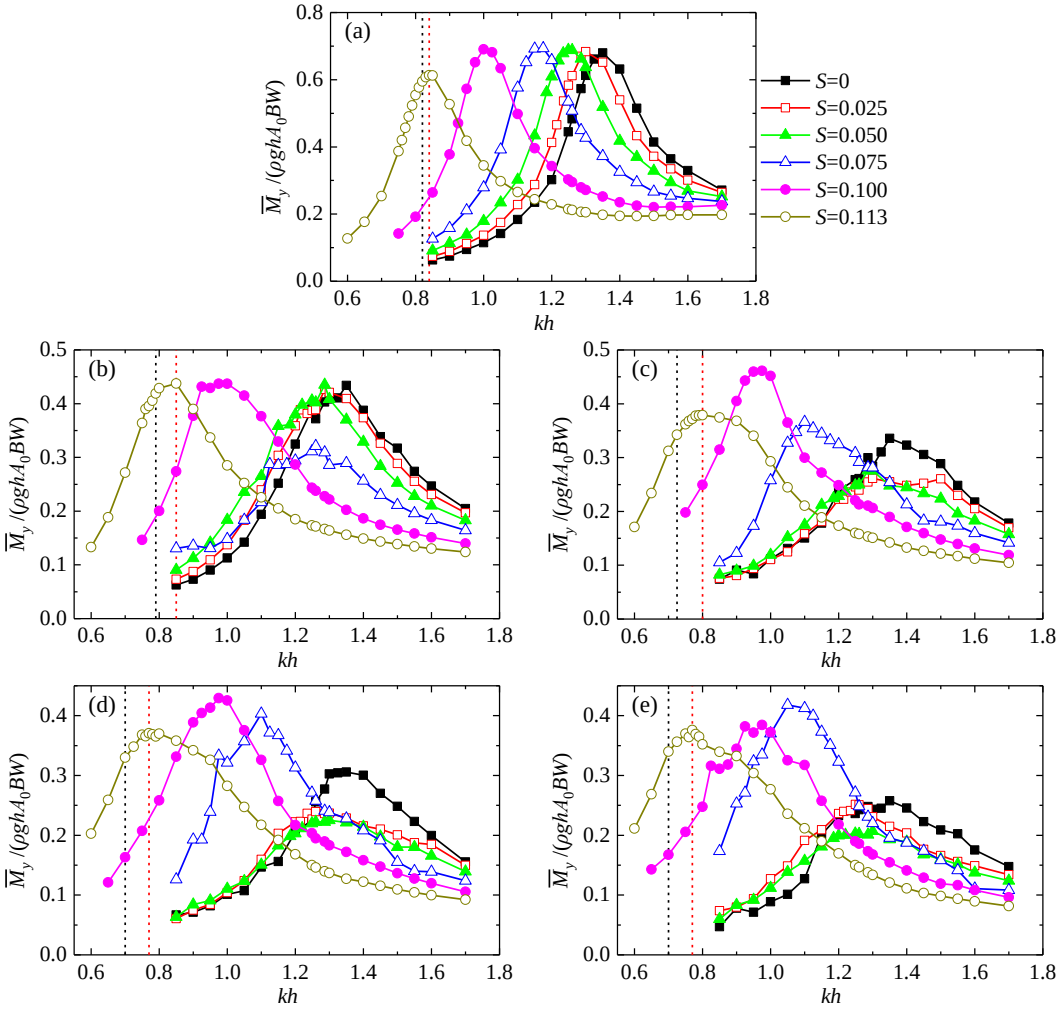

Fig. 20. Variations of the amplitude of the moment, $\overline{M}_y$, with the wave frequency under the conditions of various topographies and incident wave heights. (a)-(e) correspond to H_0=0.005 m, 0.024 m, 0.050 m, 0.075 m and 0.100 m, respectively. The black and red vertical dash lines refer to the fluid resonant frequency and the frequency at which the maximum moment appears for S=0.113, respectively.

Fig. 20 demonstrates the variations of the amplitude of the moment, $\overline{M}_y$, with the wave frequency under the conditions of various topographies and incident wave heights. The black and red vertical dash lines shown in this figure refer to the fluid resonant frequency, $(kh)_{Hg}$, and the frequency at which the maximum moment appears, $(kh)_{My}$, for the topography with S=0.113, respectively. The two phenomena that are shown in Fig. 9 for the horizontal wave force can also

be found in this figure for the moment. Firstly, for all the incident wave heights, the frequency at which the maximum moment appears, $(kh)_{My}$, is shown to decrease with the increase of the topographical slope, S, overall, which is further demonstrated in Fig. 21. Secondly, for the topography with S=0.113, there exist obvious deviations between the frequency at which the maximum moment appears, $(kh)_{My}$, and the fluid resonant frequency, $(kh)_{Hg}$. For the other topographies, similar phenomenon is also observed. Fig. 22 further illustrates the differences between $(kh)_{My}$ and $(kh)_{Hg}$ for all cases. The values of $(kh)_{My}$ are shown to be larger than those of $(kh)_{Hg}$ for almost all cases; only one case shows the equality of $(kh)_{Fx}$ and $(kh)_{Hg}$.

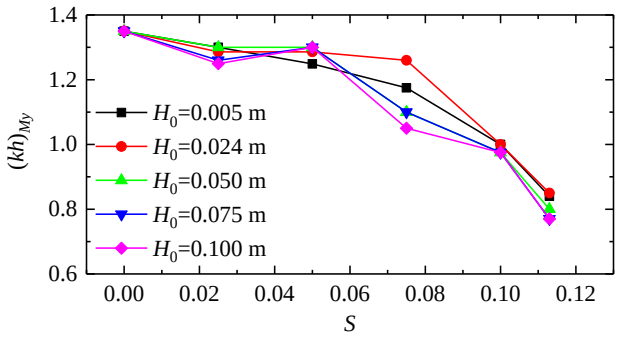

Fig. 21. The variation of the frequency at which the maximum moment appears, $(kh)_{My}$, with respect to the topographical slope, S.

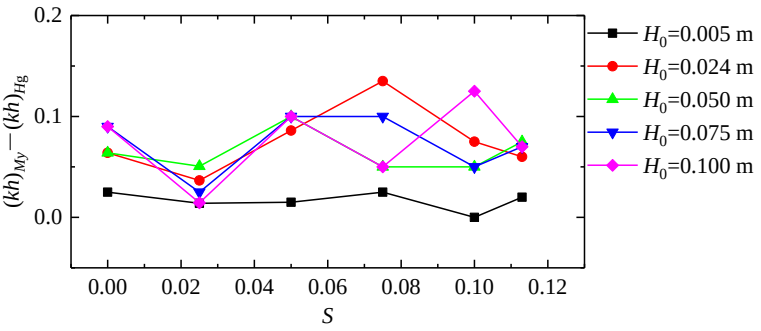

Fig. 22. The differences between $(kh)_{My}$ and $(kh)_{Hg}$ for all cases

Fig. 23 presents the variations of the maximum moment with respect to the topographical slope. Similar to the phenomenon shown in Fig. 13, for each incident wave height, the maximum moment also shows a pattern of fluctuation with the topographical slope, and the variation curve of the maximum moment also coincides well with the variation of the amplification of resonant

wave height with the slope. It indicates that apart from the horizontal wave force, the wave field inside the gap also has a dominating influence on the moment.

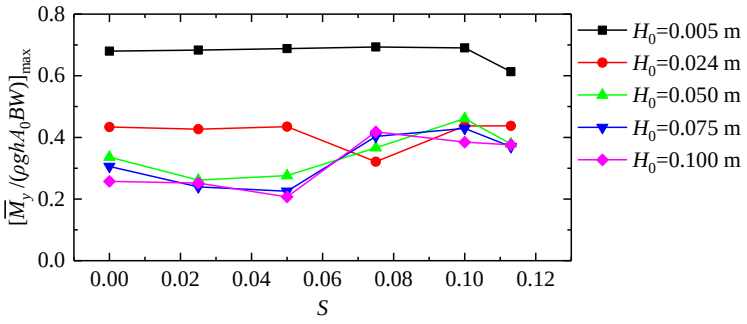

Fig. 23. The variation of the maximum moment with respect to the topographical slope, *S*.

It should be pointed out here that in general the various changing features of the maximum moment with respect to the topographical slope shown in Figs. 21-23 are very similar to the corresponding ones of the maximum horizontal wave force shown in Section 5.1. It is probably due to the following the reason. As shown in Fig. 19a and b, when the incident waves have the frequency close to the fluid resonant frequency, the positive or negative dynamic pressure is distributed among the whole bottom of the box because of the decisive influence of the wave field inside the gap. To facilitate the analysis, the pressure along the whole bottom is divided into two parts. One is distributed along the left half of the bottom and the other along the right half. It is obvious that the moments contributed by these two parts of the pressure will cancel each other out. In other words, the total moment on the box is only closely related to the pressure distributions along the left and right sides of the box which determine the horizontal wave force on the box. Hence, the general characteristics of the maximum horizontal wave force and the moment are similar.

6. Conclusions

The CFD-based numerical model, OpenFOAM®, is utilized in this study to investigate the wave loads on a fixed box during the gap resonance between the box and a vertical wall excited by the incident regular waves with different wave heights. Compared with previous investigations, the effects of the topographical variation on the wave loads during gap resonance are studied for the first time in this paper. The capability of the numerical model to accurately predict both wave

elevations and wave loads on the structure for the box-wall system is first validated against the experiments of Wang and Zou (2007). Then, the influences of the topographical variation on the wave loads, including the horizontal wave force, the vertical wave force and the moment impacting on the box during gap resonance, are investigated systematically. The results of the present research have promoted the understanding of the hydrodynamic characteristics involved in the gap resonance problem formed by large vessels berthing in front of wharfs.

The following conclusions can be drawn from the results of the present study:

1. For all the incident wave heights considered in this paper, all the frequencies at which the maximum horizontal wave force, the maximum vertical wave force and the maximum moment appear (i.e., $(kh)_{Fx}$, $(kh)_{Fz}$ and $(kh)_{My}$) are shown to decrease with the increase of the topographical slope, S, overall. These phenomena are similar to the variation of the fluid resonant frequency (i.e., $(kh)_{Hg}$) with respect to the slope, which indicates that fluid resonance in the gap has a dominating effect on the wave loads acting on the box.
2. Because of the modulation of the wave field at the left side of the box, all the values of $(kh)_{Fx}$, $(kh)_{Fz}$ and $(kh)_{My}$ present different degrees of deviations from the fluid resonant frequency, $(kh)_{Hg}$. For $(kh)_{Fx}$ and $(kh)_{My}$, the overwhelming majority of them are shown to be larger than the corresponding value of $(kh)_{Hg}$, only one or two cases show the equality between them and $(kh)_{Hg}$. While for $(kh)_{Fz}$, all of them are shown to be less than the corresponding value of $(kh)_{Hg}$.
3. For all the incident wave heights, both the maximum horizontal wave force and the maximum moment show a pattern of fluctuation with the topographical slope, and their variation curves coincide well with the corresponding variations of the amplification of resonant wave height with the topographical slope. Besides, the dimensionless maximum horizontal wave force, $[\bar{F}_x/(\rho g h A_0 W)]_{\max}$, is shown to be gradually decrease with the increase of the incident wave height. For the maximum vertical wave forces under the conditions of various incident wave heights, all of them first obviously increase and then slightly decrease with the increase of the slope, and reach the maximum values at S=0.100.

Finally, we reaffirm here that these conclusions are only valid for the given geometrical layout (including the size and draft of the box, the gap width and the water depth) and the ranges

of the topographical slope and the incident wave height studied in this article.

Acknowledgments

This research is financially supported by the National Key Research and Development Program (2017YFC1404200), the National Natural Science Foundation of China (Grant Nos. 51911530205 and 51609108) and the Jiangsu Government Scholarship for Overseas Studies (awarded to Dr. Junliang Gao for study abroad at the University of Bath). The authors also thank UK EPSRC (Grant No. EP/R007519/1), the Royal Academy of Engineering (Grant No. UK-CIAPP/73) and the Royal Society (Grant No. IEC\NSFC\181321) for providing partial support for this work.

References

Chen, X.B., 2004. Hydrodynamics in Offshore and Naval Applications (Keynote lecture), The 6th International Conference on Hydrodynamics, Perth, Austrilia.

Chua, K.H., Mello, P.d., Malta, E., Vieira, D., Watai, R., Ruggeri, F., 2018. Irregular Seas Model Experiments on Side-by-Side Barges, Proceedings of the Twenty-eighth (2018) International Ocean and Polar Engineering Conference, Sapporo, Japan, pp. 1180-1189.

Diaz-Hernandez, G., Mendez, F.J., Losada, I.J., Camus, P., Medina, R., 2015. A nearshore long-term infragravity wave analysis for open harbours. Coastal Engineering 97, 78-90.

Feng, X., Bai, W., 2015. Wave resonances in a narrow gap between two barges using fully nonlinear numerical simulation. Applied Ocean Research 50, 119-129.

Feng, X., Bai, W., 2017. Hydrodynamic analysis of marine multibody systems by a nonlinear coupled model. Journal of Fluids and Structures 70, 72-101.

Feng, X., Bai, W., Chen, X.B., Qian, L., Ma, Z.H., 2017. Numerical investigation of viscous effects on the gap resonance between side-by-side barges. Ocean Engineering 145, 44-58.

Gao, J., He, Z., Zang, J., Chen, Q., Ding, H., Wang, G., 2019a. Topographic effects on wave resonance in the narrow gap between fixed box and vertical wall. Ocean Engineering 180, 97-107.

Gao, J., Ji, C., Liu, Y., Gaidai, O., Ma, X., Liu, Z., 2016a. Numerical study on transient harbor oscillations induced by solitary waves. Ocean Engineering 126, 467-480.

Gao, J., Ma, X., Dong, G., Wang, G., Ma, Y., 2016b. Numerical study of transient harbor resonance induced by solitary waves. Proc IMechE Part M: Journal of Engineering for the Maritime Environment 230 (1), 163–176.

Gao, J., Ma, X., Dong, G., Zang, J., Zhou, X., Zhou, L., 2019b. Topographic influences on transient harbor oscillations excited by N-waves. Ocean Engineering 192, 106548.

Gao, J., Zang, J., Chen, L., Chen, Q., Ding, H., Liu, Y., 2019c. On hydrodynamic characteristics of gap resonance between two fixed bodies in close proximity. Ocean Engineering 173, 28-44.

Huang, X.H., Xiao, W., Yao, X.L., Gu, J.Y., Jiang, Z.Y., 2020. An experimental investigation of reduction effect of damping devices in the rectangular moonpool. Ocean Engineering 196, 106767.

Iwata, H., Saitoh, T., Miao, G., 2007. Fluid resonance in narrow gaps of very large floating structure composed of rectangular modules, Proceedings of the 4th International Conference on Asian and Pacific Coasts, Nanjing, China, pp. 815-826.

Jacobsen, N.G., Fuhrman, D.R., Fredsøe, J., 2012. A wave generation toolbox for the open-source CFD library: OpenFoam®. International Journal for Numerical Methods in Fluids 70 (9), 1073-1088.

Jasak, H., 1996. Error Analysis and Estimation in the Finite Volume Method with Applications to Fluid Flows. PhD thesis, Imperial College, London.

Jiang, S.-C., Bai, W., Cong, P.-W., Yan, B., 2019a. Numerical investigation of wave forces on two side-by-side non-identical boxes in close proximity under wave actions. Marine Structures 63, 16-44.

Jiang, S.-C., Bai, W., Tang, G.-Q., 2018. Numerical simulation of wave resonance in the narrow gap between two non-identical boxes. Ocean Engineering 156, 38-60.

Jiang, S.-C., Bai, W., Tang, G., 2019b. Numerical investigation of piston-modal wave resonance in the narrow gap formed by a box in front of a wall. Physics of Fluids 31, 052105.

Kumar, P., Gulshan, 2018. Theoretical analysis of extreme wave oscillation in Paradip Port using a 3-D boundary element method. Ocean Engineering 164, 13-22.

Li, B., Cheng, L., J.Deeks, A., Teng, B., 2005. A modified scaled boundary finite-element method for problems with parallel side-faces. Part II. Application and evaluation. Applied Ocean Research 27 (4-5), 224-234.

Li, Y., Zhang, C., 2016. Analysis of wave resonance in gap between two heaving barges. Ocean

Engineering 117, 210-220.

Liu, Y., Li, H.-j., 2014. A new semi-analytical solution for gap resonance between twin rectangular boxes. Proc IMechE Part M: Journal of Engineering for the Maritime Environment 228 (1), 3-16.

Lu, L., Chen, L., Teng, B., Zhao, M., 2010a. Numerical investigation of fluid resonance in two narrow gaps of three identical rectangular structures. Applied Ocean Research 32 177-190.

Lu, L., Cheng, L., Teng, B., Sun, L., 2010b. Numerical simulation and comparison of potential flow and viscous fluid models in near trapping of narrow gaps. Journal of Hydrodynamics, Ser. B 22 (5), 120-125.

Lu, L., Teng, B., Sun, L., Chen, B., 2011. Modelling of multi-bodies in close proximity under water waves—Fluid forces on floating bodies. Ocean Engineering 38 (13), 1403-1416.

Miao, G., Saitoh, T., Ishida, H., 2001. Water wave interaction of twin large scale caissons with a small gap between. Coastal Engineering Journal 43 (1), 39-58.

Molin, B., Remy, F., Kimmoun, O., Stassen, Y., 2002. Experimental study of the wave propagation and decay in a channel through a rigid ice-sheet. Applied Ocean Research 24 (5), 247-260.

Moradi, N., Zhou, T., Cheng, L., 2015. Effect of inlet configuration on wave resonance in the narrow gap of two fixed bodies in close proximity. Ocean Engineering 103, 88-102.

Morgan, G.C.J., Zang, J., 2011. Application of OpenFOAM to Coastal and Offshore Modelling, Proceedings of the 26th International Workshop on Water Waves and Floating Bodies, Athens, Greece.

Morgan, G.C.J., Zang, J., Greaves, D., Heath, A., Whitlow, C.D., Young, J.R., 2010. Using the rasInterFoam CFD model for wave transformation and coastal modeling, Proceedings of the 32nd Conference on Coastal Engineering, Shanghai, China.

Newman, J.N., 2004. Progress in wave load computations on offshore structures (Invited lecture), The 23th Conference on Offshore Mechanics and Arctic Engineering (OMAE2004), New York, USA.

Ning, D., Su, X., Zhao, M., 2016. Numerical investigation of solitary wave action on two rectangular boxes with a narrow gap. Acta Oceanologica Sinica 35 (12), 89-99.

Ning, D., Su, X., Zhao, M., Teng, B., 2015. Hydrodynamic difference of rectangular-box systems with and without narrow gaps. Journal of Engineering Mechanics 141 (8), 04015023.

Ning, D., Zhu, Y., Zhang, C., Zhao, M., 2018. Experimental and numerical study on wave response at the gap between two barges of different draughts. Applied Ocean Research 77, 14-25.

Perić, M., Swan, C., 2015. An experimental study of the wave excitation in the gap between two closely spaced bodies, with implications for LNG offloading. Applied Ocean Research 51, 320-330.

Saitoh, T., Miao, G., Ishida, H., 2006. Theoretical analysis on appearance condition of fluid resonance in a narrow gap between two modules of very large floating structure, Proceedings of the 3rd Asia-Pacific Workshop on Marine Hydrodynamics, Shanghai, China, pp. 170-175.

Sun, L., Taylor, R.E., Taylor, P.H., 2010. First- and second-order analysis of resonant waves between adjacent barges. Journal of Fluids and Structures 26 (6), 954-978.

Sun, L., Taylor, R.E., Taylor, P.H., 2015. Wave driven free surface motion in the gap between a tanker and an FLNG barge. Applied Ocean Research 51, 331-349.

Tan, L., Lu, L., Liu, Y., Sabodash, O.A., Teng, B., 2014. Dissipative Effects of Resonant Waves in Confined Space Formed by Floating Box in Front of Vertical Wall, Proceedings of the Eleventh ISOPE Pacific/Asia Offshore Mechanics Symposium, Shanghai, China. Paper No. ISOPE-P-14-080.

Tan, L., Lu, L., Tang, G.-Q., Cheng, L., Chen, X.-B., 2019. A viscous damping model for piston mode resonance. Journal of Fluid Mechanics 871, 510-533.

Wang, D.-G., Zou, Z.-L., 2007. Study of non-linear wave motions and wave forces on ship sections against vertical quay in a harbor. Ocean Engineering 34 (8-9), 1245-1256.

Wang, G., Zheng, J.-H., Maa, J.P.-Y., Zhang, J.-S., Tao, A.-F., 2013. Numerical experiments on transverse oscillations induced by normal-incident waves in a rectangular harbor of constant slope. Ocean Engineering 57, 1-10.

Zhao, W., Wolgamot, H.A., Taylor, P.H., Taylor, R.E., 2017. Gap resonance and higher harmonics driven by focused transient wave groups. Journal of Fluid Mechanics 812, 905-939.

Zhu, D.-t., Wang, X.-g., Liu, Q.-j., 2017. Conditions and phase shift of fluid resonance in narrow gaps of bottom mounted caissons. China Ocean Engineering 31 (6), 724-735.

Zhu, R., Miao, G., You, Y., 2005. Influence of gaps between 3-D multiple floating structures on wave forces. Journal of Hydrodynamics , Ser. B 17 (2), 141-147.